

Internal Dynamics, Structure and Formation of Dwarf Elliptical Galaxies: I. A Keck/HST Study of Six Virgo Cluster Dwarfs

M. Geha

UCO/Lick Observatory, University of California, Santa Cruz, 1156 High Street, Santa Cruz, CA 95064

mgeha@ucolick.org

P. Guhathakurta^{1,2}

Herzberg Institute of Astrophysics, National Research Council of Canada, 5071 West Saanich Road, Victoria, B.C., Canada V9E 2E7

raja@ucolick.org

and

R. P. van der Marel

Space Telescope Science Institute, 3700 San Martin Dr., Baltimore, MD 21218

marel@stsci.edu

ABSTRACT

Spectroscopy with the Keck II 10-meter telescope* and Echelle Spectrograph and Imager is presented for six Virgo Cluster dwarf elliptical (dE) galaxies in the absolute magnitude range $-15.7 \leq M_V \leq -17.2$. The mean line-of-sight velocity and velocity dispersion are resolved as a function of radius along the major axis of each galaxy, nearly doubling the total number of dEs with spatially-resolved stellar kinematics. None of the observed objects shows evidence of strong rotation: upper limits on v_{rot}/σ , the ratio of the maximum rotational velocity to the mean velocity dispersion, are well below those

¹Herzberg Fellow

²Permanent address: UCO/Lick Observatory, University of California, Santa Cruz, 1156 High Street, Santa Cruz, CA 95064

*Data presented herein were obtained at the W. M. Keck Observatory, which is operated as a scientific partnership among the California Institute of Technology, the University of California and the National Aeronautics and Space Administration. The Observatory was made possible by the generous financial support of the W. M. Keck Foundation.

expected for rotationally-flattened objects. Such limits place strong constraints on dE galaxy formation models. Although these galaxies continue the trend of low rotation velocities observed in Local Group dEs, they are in contrast to recent observations of large rotation velocities in slightly brighter cluster dEs. Using surface photometry from *Hubble Space Telescope*[†] Wide Field Planetary Camera 2 images and spherically-symmetric dynamical models, we determine global mass-to-light ratios $3 \leq \Upsilon_V \leq 6$. These ratios are comparable to those expected for an old to intermediate-age stellar population and are broadly consistent with the observed $(V - I)$ colors of the galaxies. These dE galaxies therefore do not require a significant dark matter component inside an effective radius. We are able to rule out central black holes more massive than $\sim 10^7 M_\odot$. For the five nucleated dEs in our sample, kinematic and photometric properties were determined for the central nucleus separately from the underlying host dE galaxy. These nuclei are as bright or brighter than the most luminous Galactic globular clusters and lie near the region of Fundamental Plane space occupied by globular clusters. In this space, the Virgo dE galaxies lie in the same general region as Local Group and other nearby dEs, although non-rotating dEs appear to have a slightly higher mean mass and mass-to-light ratio than rotating dEs; the dE galaxies occupy a plane parallel to, but offset from, that occupied by normal elliptical galaxies.

Subject headings: galaxies: dwarf — galaxies: kinematics and dynamics

1. Introduction

Dwarf elliptical galaxies (dEs) are the most common galaxy type by number in the Local Universe, dominating the galaxy luminosity function of nearby clusters. Yet these galaxies remain among the most poorly studied galaxies due to their faint luminosities, $M_V \geq -18$, and characteristic low effective surface brightness $\mu_{V,\text{eff}} > 22 \text{ mag arcsec}^{-2}$ (Ferguson & Binggeli 1994). Unlike brighter, classical elliptical galaxies whose surface brightness profiles are well fit by the de Vaucouleurs $r^{1/4}$ law (de Vaucouleurs 1948), dEs have brightness profiles that are characterized by Sérsic profiles (Sérsic 1968) with indices ranging between $n = 1-3$ (where $n = 1$ corresponds to an exponential law and $n = 4$ to an $r^{1/4}$ law) making them appear more diffuse than classical ellipticals of the same total magnitude (Binggeli & Jerjen 1998). In the Virgo Cluster, the majority of dEs brighter than $M_V \lesssim -16$ contain compact central nuclei; fainter than $M_V \gtrsim -12$ most dEs show no sign of a nucleus (Sandage, Binggeli, & Tammann 1985). Nuclei typically contain 5% to 20% of the total galaxy light and are slightly resolved at the distance of Virgo by *Hubble Space Telescope* (*HST*) imaging (Miller et al. 1998).

[†]Based on observations with the NASA/ESA Hubble Space Telescope, obtained at the Space Telescope Science Institute, which is operated by the Association of Universities for Research in Astronomy, Inc., under NASA contract NAS 5-26555.

In hierarchical models of galaxy formation, dwarf galaxies form out of small density fluctuations in the early Universe and are predicted to be less spatially clustered than normal elliptical or spiral galaxies (Dekel & Silk 1986). However, dwarf elliptical galaxies are preferentially found in dense cluster environments, more so than either ellipticals or spirals (Binggelli et al. 1987); there are few, if any, examples of isolated dEs. Thus, current models favor dE formation from a progenitor galaxy population. The proposed progenitors of dEs are spiral or irregular galaxies which are morphologically transformed into dEs through the processes of galaxy harassment and interaction (Moore, Lake, & Katz 1998). Detailed internal kinematics of dEs are a powerful observational tool with which to test these scenarios.

Until recently, radial velocity dispersion profiles were only available for the Local Group dEs and two of the brightest dEs in the Virgo Cluster (Bender & Nieto 1990; Bender, Paquet, & Nieto 1991; Held, Mould, & de Zeeuw 1990). In addition, a handful of global velocity dispersion measurements existed for dEs in various environments outside the Local Group (Peterson & Caldwell 1993). These observations suggest that dEs have lower mass-to-light ratios than Local Group dwarf spheroidals (e.g., Draco, Fornax) and are flattened by velocity anisotropy rather than by rotation. However, Pedraz et al. (2002) and de Rijcke et al. (2001) recently presented kinematic profiles for a few dEs in the Virgo and Fornax Clusters, respectively, with rotation velocities comparable to that expected for a rotationally-flattened spheroid. These rotating dEs are more luminous on average than the non-rotating dEs we have observed, and hint at a possible association between dE luminosity and the presence of rotation.

The question of whether dEs have significant rotation compared to their velocity dispersion is particularly important in the context of dE formation scenarios. Moore et al. (1998) have demonstrated that the process of galaxy harassment in cluster environments can morphologically transform a spiral galaxy into a dE. Although this process tends to increase the velocity dispersion in a system, it is less efficient at disrupting rotational motions and a significant fraction of the progenitor’s rotation is preserved. Thus, measuring the amount of internal angular momentum in dEs can constrain the progenitor galaxy type and/or the amount of disruption required.

We present internal kinematics as a function of radius for a sample of six dE galaxies in the Virgo Cluster based on Keck observations. These data are interpreted in conjunction with archival *HST* imaging. Preliminary results from this study were presented in Geha, Guhathakurta, & van der Marel (2002). This paper is organized as follows: in §2 we present the Keck spectroscopic and *HST* imaging observations of our target galaxies, along with an outline of data reduction procedures; in §3 we present velocity and velocity dispersion profiles and describe the dynamical models that are applied to the data to derive mass-to-light ratios, constraints on orbital anisotropy, and limits on the central black hole mass; the broader implications of the results are discussed in §4.

2. The Data

The Virgo Cluster is the closest large reservoir of dE galaxies beyond the Local Group and presents a significantly different environment in which to study such galaxies. The six dE galaxies presented below were drawn from the bright end of the Virgo dE luminosity function and have been imaged with *HST*. These objects lie at a variety of distances from the center of the Virgo Cluster as shown in Figure 1. The positions and photometric properties of the observed galaxies are listed in Table 1. Foreground reddening values are taken from Schlegel, Finkbeiner, & Davis (1998) assuming a standard Galactic extinction law with $R_V = 3.1$. Throughout this paper a Virgo Cluster true distance modulus of $(m - M)_0 = 30.92$ is adopted, i.e., a distance of 15.3 Mpc, as determined by the *HST* Key Project on the extragalactic distance scale (Freedman et al. 2001).

2.1. Spectroscopy

2.1.1. Observations

Six dE galaxies were observed on 2001 March 20–21 using the Keck II 10-m telescope and the Echelle Spectrograph and Imager (ESI; Sheinis et al. 2002). Observations were made in the echelle mode with continuous wavelength coverage over the range $\lambda\lambda 3900\text{--}11000\text{\AA}$ across 10 echelle orders with a spectral dispersion of $11.4\text{ km s}^{-1}\text{ pixel}^{-1}$. The spectra were obtained through a $0.75'' \times 20''$ slit, resulting in an instrumental resolution of 23 km s^{-1} (Gaussian sigma) over the entire spectrum, or $R \equiv (\lambda/\Delta\lambda) \approx 10,000$. The slit was positioned on the major axis of each galaxy, such that the galaxy’s center was displaced $\sim 5''$ from the center of the slit along its $20''$ length. Three consecutive exposures of 20 minutes were obtained for each galaxy except VCC 1577, for which 5×20 minutes were obtained. A summary of the observing parameters is given in Table 2. High signal-to-noise ratio spectra of giant stars covering the range of spectral types G8III to M0III were taken with the same instrumental setup for use as templates in the kinematic profile fitting described in § 2.1.3. Standards stars were observed both centered on and trailed across the slit width in order to recover an accurate estimate of the instrumental broadening for point and extended sources, respectively.

2.1.2. Data Reduction

The ESI data were reduced using a combination of IRAF echelle and long-slit spectral reduction tasks. First, the overscan and a dark frame, scaled by the exposure time, were subtracted from the data. The sum of a bright calibration star spectral exposure and a flat field spectral exposure were used to trace the ends of the slit as well as a fiducial spatial point (the location of the bright star) for each of the 10 curved echelle orders. This process yielded an empirical measurement of the spatial pixel scale for each order: it varies from $0.13''$ in the bluest order to $0.18''$ in the reddest

order. Scattered light was subtracted from individual frames by fitting a smooth function to the areas outside these apertures (spaces between echelle orders) using the APSCATTER task. To preserve spatial information, the APALL task was used in “strip” mode to extract and rectify two-dimensional rectangular strips for each echelle order by shifting and aligning each spatial column based on the aperture trace information. The rectified orders were then interpolated to a common spatial pixel scale of $0.18''$ per pixel. Calibration frames such as flat field, arc lamp, and template star exposures were also extracted into rectified, aligned and spatially-corrected strips using the same procedure.

Data reduction was carried out on these rectified strips using procedures similar to those routinely used on long-slit spectra. Each strip was divided by its corresponding normalized flat-field image (from the same echelle order). Cosmic rays on individual exposures, identified on the basis of object sharpness and peak pixel brightness, were masked and the exposures were then combined. Each order was logarithmically binned in wavelength using a two-dimensional wavelength calibration (i.e., as a function of spatial position along the slit) determined from a combined Cu/Ar/Hg/Ne arc lamp spectrum. The rms of the residuals in the wavelength solution is 0.05\AA or less in each order. The sky spectrum was determined for each combined frame from a section near the end of the slit farthest from the galaxy center ($r \sim 15''$), and subtracted from the rest of the two-dimensional spectrum. We recognize that this “sky” spectrum is contaminated by light from the outer parts of the target dE galaxy but this is unlikely to have a significant effect on our results.[¶] Bright, poorly-subtracted sky lines were masked out during the kinematic fitting discussed below. The galaxy continuum flux in each order was then individually normalized to unity using the IRAF CONTINUUM task. A noise frame was created for each galaxy spectrum which kept track of uncertainties in every pixel due to read noise and Poisson noise taking into account the CCD gain and number of readouts. This noise frame is used as input into the kinematic analysis of § 2.1.3 as part of the formal error calculations on the velocity profile parameters. Finally, the strips from the different echelle orders were combined, weighted by the noise frame, to create a single two-dimensional long-slit spectrum. Due to low signal-to-noise in the reddest and bluest echelle orders, we do not include them in the analysis; the final combined spectrum covers $\lambda\lambda 4800 - 9200\text{\AA}$. The spectra show no evidence for gaseous emission lines at any radii. Representative combined galaxy spectra are shown in Figure 2.

The seeing FWHM during each spectroscopic observation was determined by comparing the observed intensity profile along the ESI slit to high spatial resolution V -band surface brightness profiles derived from *HST* images (as discussed in § 2.2.1). These brightness profiles were convolved with a Gaussian seeing point spread function (PSF), integrated over the $0.75''$ slit width and binned

[¶]Based on the surface brightness profiles in Figure 4 we estimate that the “sky” spectrum is contaminated by galaxy light at the level of $\lesssim 1\%$ and $\approx 5\%$ relative to the dE’s center, with and without the nuclear contribution, respectively. In the outer parts of the dE profile ($r = 5''$), the contamination level is higher (20%–30%), but even this should not be a problem since there are no strong radial gradients in the mean velocity and velocity dispersion in the outer parts of the galaxies.

into $0.18''$ pixels to match the ESI pixel scale in the spatial direction. This was then compared to the observed intensity profile along the ESI slit in the matching spectral region. The best-fit Gaussian FWHM seeing estimates are given in Table 2 for each galaxy. These are consistent with the less accurate estimates of the seeing FWHM determined by coadding short (few second) exposures taken with the ESI guider camera at intervals of approximately 5 minutes during the spectroscopic observations.

2.1.3. *Measurement of Line-of-Sight Velocity and Velocity Dispersions*

The mean line-of-sight velocity and velocity dispersion as a function of radius were determined using a pixel-fitting method first described in van der Marel (1994). These quantities were determined by comparing the observed galaxy spectrum to a stellar template convolved with a series of Gaussian line profiles. The best-fitting Gaussian profile was determined by χ^2 minimization in pixel space. The free parameters in this analysis are: mean line-of-sight velocity v , velocity dispersion σ , and a line-strength parameter γ , which measures the ratio of equivalent width in the galaxy to that of the template star and accounts for template mismatch (e.g., due to differences in effective temperature or metallicity). Night sky absorption features (A and B bands) and strong sky emission lines were masked out in the fitting procedure; masked pixels were not included in the calculation of χ^2 . Deviations from Gaussian profiles (van der Marel & Franx 1993) were not fit as this requires higher signal-to-noise spectra than presented in this paper. In addition, an arbitrary continuum term was simultaneously fit to the data approximated by the sum of Legendre polynomials. In analyzing the combined ESI spectra ($\approx 20,000$ pixels), the continuum was fit with a 20th order polynomial.

We have tested this method on broadened template stars to determine the minimum signal-to-noise required to accurately recover velocity dispersions and to estimate our sensitivity to template mismatch. Stellar templates were broadened with Gaussian kernels of varying σ and Poisson noise was added. These tests suggest that for a signal-to-noise level $S/N \geq 10$ per spectral pixel, a galaxy’s internal velocity dispersions can be measured down to the instrumental resolution of 23 km s^{-1} with an accuracy of 1% and down to 18.5 km s^{-1} with an accuracy of 10%. We have spatially rebinned our galaxy data to achieve a signal-to-noise level of $S/N \geq 10$ per pixel at all radii, while ensuring that the spatial bin size is at least as large as the FWHM of seeing during the observations ($\sim 0.9''$). Velocity profiles were recovered using template stars ranging in spectral type G8III to M0III. The best fitting template, the K1III star HD 40460 ($[Fe/H] = -0.42$), was used to recover all profiles presented here. The choice of template star did not affect the recovered profiles at a level in excess of the formal error bars. We also find no significant difference between the profiles presented here to those determined by separately recovering profiles for the eight ESI echelle orders and computing a profile based on the weighted mean.

2.1.4. A Reliability Test: Comparison of ESI and HIRES Data

We have previously attempted to observe Virgo dE galaxies with Keck/HIRES in March 1998. The significantly higher spectral resolution of HIRES ($2.1 \text{ km s}^{-1} \text{ pixel}^{-1}$) and its lower throughput as compared to ESI made these observations prohibitively difficult. The dE galaxies VCC 1254, VCC 1073, VCC 452 and VCC 1876 were observed for 5, 3, 2 and 1.8 hours, respectively, through a custom-made $2.0'' \times 11.0''$ slit. We were able to determine the kinematics for VCC 1254 inside $r < 2''$; however, data for the last three galaxies did not have sufficient signal-to-noise to recover velocity profiles. Although this HIRES spectrum does not provide additional information on VCC 1254, it does provide an excellent reliability check on our ESI observations. The ESI and HIRES data complement each other in that the ESI data have relatively high S/N but an instrumental resolution approaching the intrinsic dispersion of our target galaxies, whereas the instrumental resolution of HIRES is significantly higher at the price of low signal-to-noise. As shown in Figure 3, the line profile shapes and velocity profiles determined with HIRES match that measured by ESI. The velocity profiles were calculated in the wavelength region $\lambda\lambda 5000\text{--}5250\text{\AA}$, however, we have no reason to believe that this agreement would be any less in other spectral regions.

2.2. Imaging

2.2.1. Observations and Data Reduction

HST Wide Field Planetary Camera 2 (WFPC2) imaging is available for each of our target galaxies. These images provide high spatial resolution surface brightness profiles needed for the dynamical modeling discussed in §3.2.1, and allowed us to measure photometric properties for our target galaxies. The data, first presented in Miller et al. (1998) and Stiavelli et al. (2001), consist of 2×230 -s WFPC2 images in the F555W bandpass and a single 300-s exposure in F814W. The galaxies are centered on the WF3 CCD in the *HST* pointings, and we use only the F555W WF3 CCD image to determine surface brightness profiles. The images were cleaned of cosmic rays and combined. The instrumental F555W magnitudes were calibrated into V -band using the transformations of Holtzman et al. (1995), assuming $(V - I) = 1.0$ (Miller et al. 1998). Surface brightness profiles were determined for each galaxy using the IRAF ELLIPSE isophotal fitting routine down to a surface brightness of $\mu_V \sim 24$. The average ellipticity, ϵ , determined between $r = 1'' - 20''$ and the total integrated apparent magnitude, determined by integrating the total flux inside a $40''$ aperture, are given in Table 1. Our apparent magnitudes agree with those determined by Miller et al. (1998). Unlike Miller et al., we consider VCC 1577 to be a nucleated dE galaxy since its bright, central star cluster is within a few tenths of an arcsecond of the galaxy’s isophotal centroid position. The observed surface brightness profiles are shown in Figure 4.

2.2.2. Surface Brightness Profile Fitting

In subsequent analysis, we differentiate between light from the central dE nucleus and the underlying galaxy. We therefore fit separate analytic profiles to the inner and outer surface brightness profiles. For the underlying galaxy, a Sersic profile is fit of the form: $I^{\text{gal}}(r) = I_0^{\text{gal}} \exp[(r/r_0)^{1/n}]$, where a Sersic index $n = 1$ represents an exponential profile and $n = 4$ is a de Vaucouleurs law. The best-fit Sersic profile is determined by non-linear least-squares fitting to the region $r = 1'' - 20''$; in this region, contributions from the nucleus and effects of the *HST* WFPC2 PSF should be negligible. The resulting profiles are shown in Figure 4, and Sersic indices and half-light effective radii are listed in Table 3. Best-fitting Sersic indices range between $n = 0.8 - 2.9$. There is a slight trend towards smaller n values (more closely exponential) at fainter magnitudes, consistent with that seen in the much larger sample of Virgo dE surface brightness profiles analyzed by Bingelli & Jerjen (1998).

At the distance of the Virgo Cluster, the nuclei of dE galaxies are slightly extended compared to the WFPC2 PSF. We have used the ISHAPE software developed by Larsen (1999) to derive shape parameters for these nuclei. The intrinsic shape of the nuclei was modeled as a Plummer profile whose projected intensity scales as $I^{\text{nuc}}(r) = I_0^{\text{nuc}}/[1 + (r/b_{\text{nuc}})^2]^2$, where b_{nuc} is the scale radius of the nucleus which, for this profile, is also the half-light radius. The ISHAPE software convolves the analytic profile with the WFPC2 F555W PSF and a diffusion kernel generated by the TinyTim software (Krist & Hook 1997), and determines the best-fitting model parameters by minimizing residuals between the model and original two-dimensional image. Nuclear profiles were fit inside the central $1.0''$ (10 pixels) and were assumed to be circularly symmetric. The free model parameters are the effective radius, b_{nuc} , the profile normalization, I_0^{nuc} , and a constant background level. Although a constant background level is a good approximation for the non-nuclear component inside the fitting radius, it is more appropriate to subtract the underlying galaxy Sersic profile. Therefore, we use the ISHAPE software to fit only the profile shape, b_{nuc} , and determine the profile normalization, I_0^{nuc} , such that the total nuclear magnitude equals the luminosity leftover after subtraction of the galaxy Sersic profile from the total observed surface brightness profile. For the five nucleated dEs, the resulting nuclear profiles are plotted as dotted lines in Figure 4; effective half-light radii and total nuclear magnitudes are given in Table 3.

3. Results

Results of the kinematic analysis of § 2.1.3 are shown for all galaxies in Figure 5; the derived kinematic profiles are summarized in Table 4. The mean line-of-sight velocity and velocity dispersion are plotted as a function of major axis radius in arcseconds; the radius was measured relative to the peak position of the intensity profile along the ESI slit. The systemic radial velocity of each dE was determined from the mean of the velocity data points and subtracted from the velocity profile. The corrected heliocentric velocities are listed in Table 4 and agree, within measurement

errors, with previously published radial velocity measurements for VCC 917, VCC 1073, VCC 1254 and VCC 1876 (Binggelli, Sandage, & Tammann 1985).

3.1. Velocity Profiles: A Lack of Rotation

The velocity profiles in Figure 5 show no evidence for substantial rotation along the major axis of any of the six dE systems observed. To quantify the maximum rotation velocity allowed by the data, we have differenced the average velocities on either side of the major axis of the galaxy and divided by two (v_{rot} in Table 4). This quantity is not particularly meaningful for galaxies which do not show a coherent rotation curve; it merely represents an upper limit on rotational motion. Error bars on rotational motion were determined by adding in quadrature the error of the mean velocity on either side of the major axis. If the observed flattening of these galaxies were determined by rotational motion alone, the expected rotation velocity can be calculated directly from the tensor virial theorem, given the observed velocity dispersion (Binney & Tremaine 1987). The ratio of the maximum rotational velocity to the average velocity dispersion (v_{rot}/σ) is plotted versus ellipticity in Figure 6 and compared to the ratio expected from an isotropic, rotationally-flattened body. Ellipticity and average velocity dispersion are determined outside $r = 1''$ in order to exclude any contributions from a central nucleus and are listed in Tables 2 and 3, respectively. The upper limits on v_{rot}/σ determined for these galaxies are significantly smaller than expected if the observed flattenings were due to rotation. Thus, from Figure 6 we conclude that these dEs are primarily flattened by anisotropic velocity dispersions.

The low rotation velocities of this study are consistent with previous measurements of dE velocity profiles in the Local Group (Bender & Nieto 1990). However, recent studies of dE kinematics suggest that a fraction of dE galaxies are rotationally supported. A rotational velocity of 15 km s^{-1} was measured by de Rijcke et al. (2001) for FS 76, a dE in the Fornax Cluster, slightly below the value expected if this system is rotationally supported. Pedraz et al. (2002) found that five of their six Virgo Cluster dEs rotated with maximum velocities between 15 to 30 km s^{-1} , placing them on or above the relation for rotational support. The sixth galaxy presented by Pedraz et al., IC 794 or VCC 1073, is also in our sample. Their measurement, $v_{\text{rot}} = 3.4 \pm 1.7 \text{ km s}^{-1}$, is consistent with our observation of low rotation velocity, $v_{\text{rot}} = 2.1 \pm 0.4 \text{ km s}^{-1}$. Thus, of the 11 Virgo dEs with measured velocity profiles, 5 have significant rotation velocities and 6 are non-rotating. We note that the average brightness of the rotating dE sample ($M_V = -17.6$, assuming $(B-V) = 0.8$ (Gavazzi et al. 2001)) is slightly brighter than that of our non-rotating dEs ($M_V = -16.4$). In § 3.3 we find that these two populations are also slightly separated in the Fundamental Plane. We have recently observed a larger sample of Virgo dE galaxies, some of which have significant rotation velocities and some which do not. We will explore in more depth the differences between these two classes in a forthcoming paper.

3.2. Interpreting Velocity Dispersion Profiles

The mean velocity dispersions of the six dE galaxies presented in Figure 5 lie between 20 and 55 km s⁻¹, and show a wide range of profile shapes. Although Virgo dE nuclei are unresolved from the ground, the kinematics of the central nucleus appear to be distinguished from the underlying galaxy. Surprisingly, the central velocity dispersion can be either larger (VCC 1254) or smaller (VCC 1073, VCC 452) than the surrounding galaxy. Below, we construct dynamical models for each of the observed galaxies in order to explore the range of mass-to-light ratios, velocity dispersion anisotropy and central black hole masses allowed by the observed profiles.

3.2.1. Dynamical Modeling

High spatial resolution WFPC2 imaging available for all of the observed dEs (§ 2.2.1) allows dynamical modeling of the velocity dispersion profiles through the assumption that the stellar mass density is proportional to the luminosity density times some mass-to-light ratio at all radii. Solving the spherically symmetric Jeans equation, the predicted kinematics are convolved through the observational setup, allowing a direct comparison to the observations. The simplifying assumption of spherical symmetry is justified as more generalized models cannot be discriminated against without additional information such as minor axis kinematics or higher order velocity profile moments. We produce spherical models in which the radius is related to the observed semimajor/semiminor axes and ellipticity of the corresponding dE galaxy via the relation: $r = \sqrt{ab} = a\sqrt{1 - \epsilon}$. The square root of the product of the semi-major and minor axis is a more appropriate quantity than the semi-major axis for these elliptical systems. The models are based on dynamical software described in more detail by van der Marel (1994).

The luminosity density, $j(r)$, is determined for each galaxy by Abel transformation of the projected WFPC2 *V*-band surface brightness profile measured in § 2.2.1. To avoid noise amplification, the observed surface brightness profiles were first fit to an arbitrary function, a generalization of the “Nuker law” (Lauer et al. 1995), as shown in Figure 4. The total luminosity density is assumed to be composed of two parts, $j(r) = j_{\text{nuc}}(r) + j_{\text{gal}}(r)$, representing the central nucleus and underlying galaxy, respectively. We model the nuclear component as a Plummer model with fixed scale length, b_{nuc} , and total nuclear luminosity, L_{nuc} in the *V* band, as determined for each galaxy from the projected luminosity density in § 2.2.2. The luminosity density of a Plummer model, taken from Dejonghe (1987), is:

$$j_{\text{nuc}}(r) = \frac{3L_{\text{nuc}}}{4\pi b_{\text{nuc}}^3} \left[1 + \frac{r^2}{b_{\text{nuc}}^2} \right]^{-5/2} \quad (1)$$

The luminosity density of the underlying galaxy, $j_{\text{gal}}(r)$, is the total luminosity density minus the contribution from the nucleus. The mass density of stars, $\rho(r)$, is modeled as the luminosity density times a mass-to-light ratio. In our models, we allow two distinct mass-to-light ratios as free parameters, Υ_{gal} and Υ_{nuc} , for the underlying galaxy and nuclear component. The mass density

distribution of the galaxy component is then: $\rho_{\text{gal}}(r) = \Upsilon_{\text{gal}} j_{\text{gal}}(r)$. The mass density distribution of the nucleus is similarly defined as: $\rho_{\text{nuc}}(r) = \Upsilon_{\text{nuc}} j_{\text{nuc}}(r)$. The total mass density of the system is the sum of these densities: $\rho(r) = \Upsilon_{\text{nuc}} j_{\text{nuc}}(r) + \Upsilon_{\text{gal}} j_{\text{gal}}(r)$. Rearranging terms, the total density is modeled as:

$$\rho(r) = \Upsilon_{\text{gal}} j(r) + [(\Upsilon_{\text{nuc}} - \Upsilon_{\text{gal}}) j_{\text{nuc}}(r)] \quad (2)$$

where the total luminosity density $j(r)$ is inferred from the *HST* WFPC2 surface brightness profile, $j_{\text{nuc}}(r)$ is given in Eqn. (1), and the mass-to-light ratios Υ_{nuc} and Υ_{gal} are free parameters. The case where $\Upsilon_{\text{nuc}} = \Upsilon_{\text{gal}}$ is equivalent to the mass density of the galaxy being equal to the luminosity density times a constant mass-to-light ratio.

The total gravitational potential, Φ , is obtained by integrating over the mass density determined by Eqn. (2) plus an added possible contribution, GM_{BH}/r , from a central black hole. The velocity dispersion as a function of radius, σ_r , is then obtained by solving the spherically-symmetric Jeans equation:

$$\frac{d(\rho\sigma_r^2)}{dr} + 2\frac{\beta\rho\sigma_r^2}{r} = -\rho\frac{d\Phi}{dr} \quad (3)$$

where $\beta = 1 - \sigma_\theta^2/\sigma_r^2$ describes the velocity dispersion anisotropy. Models with $\beta = 0$ are isotropic, $\beta < 0$ are tangentially anisotropic, and $0 < \beta \leq 1$ are radially anisotropic. The radial velocity dispersion σ_r is numerically evaluated for any combination of β , M_{BH} , Υ_{gal} , Υ_{nuc} , and surface brightness profile. In order to compare to observations, the velocity dispersions are projected along the line-of-sight. The projected dispersions are convolved using Monte Carlo integration with a Gaussian kernel to take into account the seeing FWHM (as determined in § 2.1.2). The dispersions are then sampled using the slit width, pixel size, and rebinning scheme specific to each observation. The predicted dispersion $\sigma(r)$ can be compared directly to the observed velocity dispersions σ_i over all radial bins r_i by the defined quantity:

$$\chi_\sigma^2 = \left[\frac{\sigma_i - \sigma(r_i)}{\Delta\sigma_i} \right]^2 \quad (4)$$

The best-fitting model is determined by minimization of χ_σ^2 . Given the well known degeneracy between the mass profile and velocity anisotropy, and given the quality of our data, we choose not to explore the full range of allowed parameter space. Instead, we consider three limiting cases: (1) constant mass-to-light ratio and velocity anisotropy, (2) the same model plus a central black hole, and (3) models with separate mass-to-light ratios for the nucleus and underlying galaxy and no central black hole.

3.2.2. Mass-to-Light Ratios and Orbital Anisotropy

We first consider models without a central black hole for which the free parameters are a single mass-to-light ratio Υ_V (i.e. $\Upsilon_{\text{gal}} = \Upsilon_{\text{nuc}}$) and velocity dispersion anisotropy, β , both independent of radius. For each galaxy, models were run for values of the velocity dispersion anisotropy ranging

between $-3 \leq \beta \leq 0.75$. Best fitting values of β and Υ_V were determined by overall minimization of χ_σ^2 and are listed in Table 4. Formal 1σ (68% confidence) error bars are calculated for each individual free model parameter by the variation needed to increase χ_σ^2 by 1 with respect to its minimum value (Press et al. 1992). Best-fit models, as well as several representative β -value models are plotted over the observed data points in Figure 7. Although isotropic models ($\beta = 0$) do not fit the observed profiles in detail, such models do in general reproduce the dip or rise in the central dispersion observed in all six dE galaxies. Most of the galaxies are best fit with tangential anisotropy. In some cases, the amount of anisotropy needed to fit the profiles is unphysically large, motivating the models described in § 3.2.4.

The V -band mass-to-light ratios determined for our six Virgo dEs range between $3 \leq \Upsilon_V \leq 6$. These mass-to-light ratios are plotted against the absolute total magnitude of each galaxy in Figure 8 and compared to higher luminosity classical elliptical galaxies of Magorrian et al. (1998). The Magorrian et al. galaxies show a clear trend of decreasing mass-to-light ratio towards fainter magnitudes. The observed dEs tend to have larger mass-to-light ratios at a given absolute magnitude than expected by extrapolation of this relationship.

Combining the WFPC2 colors of these dE galaxies with the dynamically determined mass-to-light ratios, it is possible to roughly determine ages and metallicities for these galaxies. The colors of the six dEs lie in the range $1.0 \leq (V - I) \leq 1.2$, as measured by Stiavelli et al. (2001) from WFPC2 data averaged inside $r \leq 10''$. Approximating the stellar populations of these dEs galaxies by a single-burst population (Worthey 1994), the ages and metallicities implied by the above combined constraints lie between 5 to 12 Gyr and $-1 \leq [\text{Fe}/\text{H}] \leq 0$ dex, respectively. This rough calculation suggests that the mass determined from the observed kinematics can be accounted for by stellar populations alone without the need for a significant dark matter component, at least inside the radius of our observations (≈ 1 effective radius). This does not rule out a significant dark matter component at larger radii. Accurate determination of the ages and metallicities of these galaxies requires a rigorous analysis of their line strengths and will be presented in a forthcoming paper.

3.2.3. Upper Limits on the Mass of a Central Black Hole

We next allow an additional free model parameter in the form of a central black hole with the goal of placing upper limits on the black hole mass allowed by our kinematic data. If, for example, dEs are the morphologically-transformed remnants of larger progenitor galaxies, limits on the central black hole mass can place potentially interesting constraints on such a progenitor population. Models were run for a two-dimensional grid of velocity anisotropy versus black hole mass. For each grid point, the best fitting mass-to-light ratio is determined. Contours of constant $\Delta\chi_\sigma^2$ are shown for these two parameters in Figure 9. Confidence intervals were assigned to $\Delta\chi_\sigma^2$ values in a two dimensional parameter space, as discussed in Press et al. (1992). Black hole masses greater than $M_{\text{BH}} > 10^7 M_\odot$ can be ruled out at the 99.9% confidence level. For most objects, a zero mass black hole model is either the best fitting model, or statistically similar to the best

fit at the 90% confidence level (1.7σ). The galaxy VCC 1254 is the only dE in which a non-zero black hole mass, $M_{\text{BH}} = 9 \times 10^6 M_{\odot}$, is a significantly better fit to the data than models without a central black hole. This does not necessarily imply the presence of a black hole, as we will show below that this profile is equally well fit by a model in which the mass-to-light ratio of the nucleus is larger than the underlying galaxy. In addition, although the upper limits on black hole mass determined in this section are robust, actual black hole mass determinations would require more complicated models which allow β variations with radius. Upper limits on central dE black hole mass are compared, in Figure 10, to the black hole mass-bulge velocity dispersion relationship, $M_{\text{BH}} - \sigma_e$, derived for bulge-dominated galaxies (Gebhardt et al. 2000; Ferrarese & Merritt 2000; Tremaine et al. 2002). Although this relationship may not be applicable to dE galaxies, which lack a bulge component, our upper limits are still consistent with the relationship. The implication of these upper limits on possible dE progenitor galaxies is discussed in § 4.

3.2.4. Nuclear versus Galaxy Mass-to-Light Ratios

The kinematic profiles of the five nucleated dEs in Figure 5 show that the nuclei tend to have velocity dispersions distinct from the surrounding galaxy. In addition, photometric studies suggest that dE nuclei tend to have different colors than the underlying light of the host dE galaxy (Stiavelli et al. 2001; Durell 1997). Motivated by these observations, we consider models allowing two distinct mass-to-light ratios, one for the nucleus, Υ_{nuc} , and another for the underlying galaxy, Υ_{gal} . We explore only isotropic models ($\beta = 0$) and search for combinations of Υ_{gal} , Υ_{nuc} which minimize χ_{σ}^2 . For VCC 1254, in which the nuclear dispersion is larger than the surrounding galaxy, the best fit nuclear mass-to-light ratio is twice that for the surrounding galaxy ($\Upsilon_{\text{nuc}} = 2.1\Upsilon_{\text{gal}}$). This model fits the data equally well as the models presented in the previous two sections. However, a larger nuclear mass-to-light ratio implies an older, and therefore redder, stellar population, contrary to observations that the nucleus of VCC 1254 is bluer than the surrounding galaxy (Stiavelli et al. 2001; Durell 1997). The true dynamical state of VCC 1254 is likely to lie between the three extreme models presented in this and previous sections.

For the four nucleated galaxies in which the velocity dispersion dips in the central regions (VCC 452, VCC 1073, VCC 1577, and VCC 1876), a smaller nuclear mass-to-light ratio ($\Upsilon_{\text{nuc}} < \Upsilon_{\text{gal}}$) is only a marginally better fit to the data. In these four systems, we are not able to directly constrain the nuclear mass-to-light ratio. Even the unphysical case in which the nucleus contributes no mass, isotropic models are inadequate fits to the profiles of VCC 452 and VCC 1073, implying that these galaxies must have some degree of tangential velocity anisotropy. Isotropic, single mass-to-light ratio models are adequate fits to the profiles of VCC 1577 and VCC 1876, and variations in Υ_{nuc} do not significantly improve the fit. This can be understood because the nuclear component does not dominate the observed spectroscopic light of these galaxies, not even in the central data point. Inside $r < 1''$, the nucleus contributes between 5% and 25% of the total light in this region, as compared to 60% for VCC 1254. Thus, the measured central velocity dispersion is not a good

estimate of the velocity dispersion of the nucleus. In order to place these nuclei on the Fundamental Plane (see §3.3.2), we do need an estimate of the nuclear velocity dispersions. For this, we assume a nuclear mass-to-light ratio equal to the galaxy ($\Upsilon_{\text{nuc}} = \Upsilon_{\text{gal}}$) and calculate the central projected velocity dispersion for a Plummer model (Dejonghe 1987) with total luminosity and scale radius as determined in §2.2.2. The resulting nuclear velocity dispersions are given in Table 4.

3.3. The Fundamental Plane

In the multivariate space defined by central velocity dispersion, σ_0 , effective surface brightness, μ_{eff} , and effective radius, r_{eff} , dE galaxies occupy a region of the so-called Fundamental Plane distinct from classical elliptical galaxies. The separation is best demonstrated by the κ -space projection of this parameter space defined by Bender, Burstein, & Faber (1992) as:

$$\kappa_1 \equiv (\log[\sigma_0^2] + \log r_{\text{eff}})/\sqrt{2} \quad (5)$$

$$\kappa_2 \equiv (\log[\sigma_0^2] + 2 \log I_{\text{eff}} - \log r_{\text{eff}})/\sqrt{6} \quad (6)$$

$$\kappa_3 \equiv (\log[\sigma_0^2] - \log I_{\text{eff}} - \log r_{\text{eff}})/\sqrt{3} \quad (7)$$

where I_{eff} is defined as $10^{-0.4(\mu_{\text{eff}} - 27)}$ and is the mean intensity inside the radius r_{eff} . These coordinates are related to physical quantities as follows: κ_1 is proportional to the logarithm of mass, κ_2 is proportional to the effective surface brightness times mass-to-light ratio and κ_3 is proportional to the logarithm of mass-to-light ratio. To compare the location of our dEs in the Fundamental Plane to other galaxy types, we plot data compiled by Burstein et al. (1997) for classical ellipticals, spiral bulges, previously observed dEs, dwarf spheroidals and globular clusters. These data have been compiled in the B -band. For comparison, we transform our dE data to the B -band assuming $(B - V) = 0.8$ (Gavazzi et al. 2001). In addition, we add four of the five rotating dE galaxies presented by Pedraz et al. (2002) for which photometric data is available. Photometric properties for UGC 7436/VCC 543 were determined from WFPC2 imaging as in §2.2.2. The properties of the remaining objects were taken from Bender et al. (1992).

3.3.1. dE Galaxies in the Fundamental Plane

As seen in the edge-on, κ_1 vs. κ_3 , view of the Fundamental Plane (lower left panel, Fig. 11) dwarf ellipticals appear to lie in a plane parallel to, but offset from classical ellipticals. In the face-on, κ_1 vs. κ_2 , view (upper left panel, Fig. 11), dEs lie in a very different region of this plane, on a sequence perpendicular to the locus of classical ellipticals. The offset in κ_3 was first noted by Bender et al. (1992) and can be interpreted as either non-homology between dwarf and classical ellipticals or as a difference in mass-to-light ratios. We have shown in Figure 8 that dEs tend to have larger mass-to-light ratios at a given absolute magnitude compared to classical ellipticals, favoring the latter interpretation of the κ_3 offset. Comparing our non-rotating dEs to the rotating

dEs of Pedraz et al. (2002), these two groups lie in slightly different regions of the Fundamental Plane. The rotating dEs lie at larger κ_1 and κ_3 than the non-rotating sample, suggesting that they have both higher masses and mass-to-light ratios. From the location of the rotating dEs in the Fundamental Plane, these galaxies are not part of the low luminosity extension of classical ellipticals known to be rotationally-supported (Davies et al. 1983). Thus, dEs appear to have a wider range of rotational properties than previously assumed. The separation in both luminosity and Fundamental Plane space between these two samples suggests a correlation between rotation and another physical quantity, possibly mass. However, more data is required to establish such a correlation.

3.3.2. *dE Nuclei in the Fundamental Plane*

In the right panels of Figure 11, the nuclei of the five observed nucleated dEs are plotted. Unlike the underlying dE galaxies in the Fundamental Plane, dE nuclei lie nearest to the region occupied by globular clusters. These κ -space parameters were calculated using central velocity dispersions determined directly from a Plummer model fit to the nucleus. This is a more accurate estimate of the nuclear velocity dispersion than the measured central velocity dispersion, but requires the assumption that the nuclear mass-to-light ratio equals that of the galaxy, as discussed in §3.2.4. This assumption most strongly affects values of κ_3 . However, for any reasonable assumed nuclear mass-to-light ratio, the dE nuclei lie closest to globular clusters in the all three κ indices. The absolute luminosities of these dE nuclei ($-8.5 \leq M_V \leq -12.3$) are as bright or brighter than the most luminous Galactic globular clusters (Djorgovski 1993; Harris 1996). The nuclear effective radii are also larger than an average Galactic globular cluster, but are smaller than the largest known globulars. The resulting central luminosity densities of dE nuclei, determined from the Plummer models, are comparable to the average globular cluster central luminosity density. The position of the best studied dE nucleus, that of the Local Group dE NGC 205, a well-resolved supermassive star cluster of intermediate age and absolute magnitude $M_V = -9.6$ (Jones et al. 1996), is also plotted on the Fundamental Plane. This nucleus lies squarely in the region occupied by globular clusters. The offset position of the Virgo dE nuclei, particularly in the face-on view of the Fundamental Plane (top right panel Fig. 11), relative to Galactic globular clusters is most likely due to larger nuclear masses.

4. Discussion and Conclusions

Velocity and velocity dispersion profiles are presented for the major axes of six dE galaxies in the Virgo Cluster. These galaxies do not show evidence for substantial rotation; upper limits on rotation velocities are well below that expected if these objects were rotationally flattened. Dynamical models for these galaxies suggest mass-to-light ratios in the range $3 \leq \Upsilon_V \leq 6$. We argue that such ratios are expected for intermediate to old stellar populations and thus these dEs

do not require significant dark matter inside an effective radius. Our observations do not rule out significant dark matter in dEs at larger radii as demonstrated by giant elliptical galaxies which exist in massive dark halos, but are not necessarily dark matter dominated at small radii (Gerhard et al. 2001). In Fundamental Plane space, we find that the Virgo dE galaxies, similar to previously observed dEs, lie in a plane parallel to, but offset from, that occupied by normal elliptical galaxies. In this space, dE nuclei lie near the region occupied by Galactic globular clusters.

The origin of nuclei in dE galaxies remains an open question. In the present sample, there is no obvious difference between the single non-nucleated dE galaxy (VCC 917) and the underlying galaxies of the observed nucleated dEs. The mass-to-light ratio, anisotropy, and photometric parameters measured for VCC 917 are indistinguishable from those determined outside the nucleus of the other five dEs. However, as a population, non-nucleated dE galaxies in the Virgo Cluster do have different properties. They are observed to be less spatially concentrated, have lower specific globular cluster frequencies, and, on average, have flatter shapes as compared to nucleated dE galaxies (Sandage, Bingelli, & Tammann 1985; Miller et al. 1998; Ryden et al. 1999). Proposed scenarios for the origin of dE nuclei include the remnant cores of larger stripped galaxies (Gerola et al. 1983), the results of gas infall and star formation or the coalescence of several globular clusters whose orbits have decayed to the dE center (Oh & Lin 2000). We have shown that the observed dE nuclei share many properties with globular clusters, suggesting similar formation processes.

Since dE galaxies are preferentially found in dense environments, it is likely that galaxy interactions play a large role in their formation and evolution. The models of Moore et al. (1998) suggest that galaxy harassment in clusters can morphologically transform a spiral galaxy into a dwarf elliptical. Harassment tends to increase internal velocity dispersions, but is less efficient in disrupting rotational motion and is not obviously reconciled with the low rotational velocities observed in the present dE sample. If dEs are the morphologically-transformed remnants of larger progenitor galaxies, a constraint on such a progenitor population is provided by the central black hole mass limits determined in §3.2.3. The upper limit of $\sim 10^7 M_\odot$ for the observed dE galaxies implies that any dE progenitor must have had a bulge dispersion less than 100 km s^{-1} , assuming the $M_{\text{BH}} - \sigma_e$ relation (Tremaine et al. 2002). Although this is not a stringent constraint on dE galaxy formation models, higher spatial resolution kinematics, and therefore more stringent mass limits, could be a significant constraint on such models.

As the number of dE galaxies with measured internal kinematics increases, their position in the Fundamental Plane strengthens the conclusion that dwarf and classical elliptical galaxies evolve via very different physical processes. To determine whether dwarf ellipticals as a galaxy class evolve under homogeneous conditions requires more observations. A critical question is understanding the apparent dichotomy between the anisotropy-supported dEs presented in this paper and the rotationally-supported dEs presented by Pedraz et al. (2002) and de Rijcke et al. (2001). The fact that rotating and non-rotating dEs appear to form a “sequence” in Fundamental Plane space, with the latter having somewhat lower mean luminosity, mass, and mass-to-light ratio, suggests that these are not two distinct types of dE galaxies but rather are part of a continuous family. Larger

samples are required to establish what, if any, physical property correlates with the observed rotational velocities and what this implies for dE galaxy formation.

We would like to thank Dennis Zaritsky, Ruth Peterson and Doug Lin for help with the Keck/HIRES data discussed in §2.1.4. We are grateful to Bryan Miller for making his reduced *HST* WFPC2 images available to us and to Soeren Larsen for help with the ISHAPE software. M.G. acknowledges support from the STScI Director’s Discretionary Research Fund.

REFERENCES

- Bender, R., Burstein, D., & Faber, S. M. 1992, *ApJ*, 399, 462
- Bender, R., & Nieto, J.-L. 1990, *A&A*, 239, 97
- Bender, R., Paquet, A., & Nieto, J.-L. 1991, *A&A*, 246, 349
- Binggeli, B., & Jerjen, H. 1998, *A&A*, 333, 17
- Binggeli, B., Sandage, A., & Tammann, G. A. 1985, *AJ*, 90, 1681
- Binggeli, B., Tammann, G. A., & Sandage, A. 1987, *AJ*, 94, 251
- Binney, J., & Tremaine, S. 1987, *Galactic Dynamics*, Princeton University Press, Princeton
- Burstein, D., Bender, R., Faber, S. M., & Nolthenius, R. 1997, *AJ*, 114, 1365
- Davies, R. L., Efstathiou, G., Fall, S. M., Illingworth, G., & Schechter, P. L. 1983, *ApJ*, 266, 41
- Dejonghe, H. 1987, *MNRAS*, 224, 13
- Dekel, A., & Silk, J. 1986, *ApJ*, 303, 39
- de Vaucouleurs, G. 1948, *Ann. d’Astrophys.*, 11, 247
- Djorgovski, S. G. 1993, in “Structure and Dynamics of Globular Clusters”, ed. S. G. Djorgovski and G. Meylan (San Fransisco: ASP), 373
- Durell, P. R. 1997, *AJ*, 113, 531
- Ferrarese, L., & Merritt, D. 2000, *ApJ*, 539, L9
- Ferguson, H. C., & Binggeli, B. 1994, *A&A Rev.*, 6, 67
- Freedman, W. L., Madore, B. F., Gibson, B. K., Ferrarese, L., Kelson, D. D., Sakai, S., Mould, J. R., Kennicutt, R. C., Jr., Ford, H. C., Graham, J. A., Huchra, J. P., Hughes, S. M. G., Illingworth, G. D., Macri, L. M., & Stetson, P. B. 2001, *ApJ*, 553, 47

- Gavazzi, G., Zibetti, S., Boselli, A., Franzetti, P., Scodreggio, M., & Martocchi, S. 2001, *A&A*, 372, 29
- Gebhardt, K., Bender, R., Bower, G., Dressler, A., Faber, S. M., Filippenko, A. V., Green, R., Grillmair, C., Ho, L. C., Kormendy, J., Lauer, T., Magorrian, J., Pinkney, J., Richstone, D., & Tremaine, S. 2000, *ApJ*, 539, L13
- Geha, M., Guhathakurta P., & van der Marel, R. P. 2002, in “The Shapes of Galaxies and their Halos”, ed. P. Natarajan, World Scientific, in press (astro-ph/0107010)
- Gerhard, O., Kronawitter, A., Saglia, R. P., & Bender, R. 2001, *AJ*, 121, 1936
- Gerola, H., Carnevali, P., & Salpeter, E. E. 1983, *ApJ*, 268, L75
- Harris, W. E. 1996, *AJ*, 112, 1487
- Held, E. V., Mould, J. R., & de Zeeuw, P. T. 1990, *AJ*, 100, 415
- Holtzman, J. A., Burrows, C. J., Casertano, S., Hester, J. J., Trauger, J. T., Watson, A. M., & Worthey, G. 1995, *PASP*, 107, 1065
- Jones, D. H., Mould, J. R., Watson, A. M., Grillmair, C., Gallagher, J. S., Ballester, G. E., Burrows, C. J., Casertano, S., Clarke, J. T., Crisp, D., Griffiths, R. E., Hester, J. J., Hoessel, J. G., Holtzman, J. A., Scowen, P., Stapelfeldt, K. R., Trauger, J. T., & Westphal, J. A. 1996, *ApJ*, 466, 742
- Krist, J., & Hook, R. 1997, *The TinyTim User’s Guide* (Baltimore: STScI)
- Larsen, S. S. 1999, *A&A Suppl.*, 139, 393
- Lauer, T. R., Ajhar, E. A., Byun, Y.-I., Dressler, A., Faber, S. M., Grillmair C., Kormendy, J., Richstone, D., & Tremaine, S. 1995, *AJ*, 110, 2622
- Magorrian, J., Tremaine, S., Richstone, D., Bender, R., Bower, G., Dressler, A., Faber, S. M., Gebhardt, K., Green, R., Grillmair, C., Kormendy, J., & Lauer, T. 1998, *AJ*, 115, 2285
- Mayer, L., Governato, F., Colpi, M., Moore, B., Quinn, T., Wadsley, J., Stadel, J., & Lake, G. 2001, *ApJ*, 559, 754
- Miller, B. W., Lotz, J. M., Ferguson, H. C., Stiavelli, M., & Whitmore, B. C. 1998, *ApJ*, 508, L133
- Moore, B., Lake, G., & Katz, N. 1998, *ApJ*, 495, 139
- Oh, K. S., & Lin, D. N. C. 2000, *ApJ*, 543, 620
- Pedraz, S., Gorgas, J., Cardiel, N., Sanchez-Blazquez, P., & Guzman, R. 2002, *MNRAS*, 332, L59
- Peterson, R. C., & Caldwell, N. 1993, *AJ*, 105, 1411

- Press, W. H., Teukolsky, S. A., Vetterling, W. T., Flannery, B. P. 1992, *Numerical Recipes*, Cambridge University Press, Cambridge, §15.6
- de Rijcke, S., Dejonghe, H., Zeilinger, W. W., & Hau, G. K. T. 2001, *ApJ*, 559, L21
- Ryden, B., Terndrup, D. M., Pogge, R. W., & Lauer, T. R. 1999, *ApJ*, 517, 650
- Sandage, A., Binggeli, B., & Tammann, G. 1985, *AJ*, 90, 1759
- Schlegel, D. J., Finkbeiner, D. P., & Davis, M. 1998, *ApJ*, 500, 525
- Sérsic, J. L. 1968, *Atlas de Galaxias Australes* (Córdoba: Obs. Astron., Univ. Nac. Córdoba)
- Sheinis, A. I., Bolte, M., Epps, H. W., Kibrick, R. I., Miller, J. S., Radovan M. V., Bigelow, B. C., & Sutin, B. M. 2002, *PASP*, 114, 851
- Stiavelli, M., Miller, B. W., Ferguson, H. C., Mack, J., Whitmore, B. C., & Lotz, J. M. 2001, *AJ*, 121, 1385
- Tremaine, S., Gebhardt, K., Bender, R., Bower, G., Dressler, A., Faber, S. M., Filippenko, A. V., Green, R., Grillmair, C., Ho, L. C., Kormendy, J., Lauer, T. R., Magorrian, J., Pinkney, J., & Richstone, D. 2002, *ApJ*, 574, 740
- van der Marel, R. P. 1994, *MNRAS*, 270, 271
- van der Marel, R. P., & Franx, M. 1993, *ApJ*, 407, 525
- Worthey, G. 1994, *ApJS*, 95, 107

Table 1. Observed Virgo Dwarf Elliptical Galaxies: Basic Properties

Galaxy	α (J2000) (h:m:s)	δ (J2000) ($^{\circ}$:': $''$)	Type	ϵ	m_V	A_V	$M_{V,0}$
VCC 452	12:21:04.7	11:45:18	dE4,N	0.08	15.34	0.09	−15.67
VCC 917/IC 3344	12:26:32.4	13:34:43	dE6	0.45	13.93	0.11	−17.10
VCC 1073/IC 794	12:28:08.6	12:05:36	dE3,N	0.30	13.82	0.09	−17.19
VCC 1254	12:30:05.3	08:04:29	dE0,N	0.05	14.58	0.07	−16.41
VCC 1577	12:34:38.4	15:36:10	dE4,N	0.17	15.24	0.09	−15.77
VCC 1876/IC 3658	12:41:20.4	14:42:02	dE5,N	0.23	14.65	0.10	−16.37

Note. — Galaxy classifications taken from Bingelli et al. (1985). The ellipticity ϵ is measured between $1'' < r < 20''$; apparent and absolute magnitudes are determined inside an $r < 40''$ aperture. The absolute magnitudes, $M_{V,0}$, assume a Virgo Cluster distance modulus of $(m - M)_0 = 30.92$ and are corrected for reddening.

Table 2. Spectroscopic Observing Parameters

Galaxy	Exposure Time (s)	PA _{maj} ($^{\circ}$)	Seeing FWHM ($''$)
VCC 452	3600	−34	1.1
VCC 917/IC 3344	3600	52	0.9
VCC 1073/IC 794	3600	−60	0.8
VCC 1254	3600	0	0.8
VCC 1577	6000	20	1.0
VCC 1876/IC 3658	3600	68	1.0

Table 3. Surface Photometry Results

Galaxy	r_{eff} [$''$ (kpc)]	$\mu_{V,\text{eff}}$ (mag arcsec $^{-2}$)	n_{Sersic}	b_{nuc} [$''$ (kpc)]	$\mu_{V,\text{eff}}^{\text{nuc}}$ (mag arcsec $^{-2}$)	m_V^{nuc}	$M_{V,0}^{\text{nuc}}$
VCC 452	9.6 (0.71)	22.3	1.6	0.15 (0.011)	20.7	22.54	−8.47
VCC 917/IC 3344	12.2 (0.90)	21.4	2.9
VCC 1073/IC 794	11.1 (0.82)	21.1	1.9	0.13 (0.010)	17.4	19.86	−11.15
VCC 1254	14.4 (1.07)	22.4	2.9	0.17 (0.013)	16.7	18.67	−12.32
VCC 1577	10.5 (0.78)	22.4	1.1	0.16 (0.011)	20.1	22.23	−8.78
VCC 1876/IC 3658	10.5 (0.78)	21.8	0.8	0.11 (0.008)	17.9	20.92	−10.10

Note. — The effective half-light radius r_{eff} , effective surface brightness $\mu_{V,\text{eff}}$, and index n_{Sersic} are determined by fitting a Sersic model to the galaxy surface brightness profile outside $r > 1''$. The effective half-light radius b_{nuc} , effective surface brightness $\mu_{V,\text{eff}}^{\text{nuc}}$, and total magnitude of the nucleus are determined only for the nucleated dEs by fitting a Plummer model to the inner ($r < 1''$) brightness profile via deconvolution using the ISHAPE software (Larsen 1999) as explained in §2.2.2.

Table 4. Results of Kinematical Analysis / Dynamical Modeling

Galaxy	v_{sys} (km s ⁻¹)	v_{rot} (km s ⁻¹)	σ_{gal} (km s ⁻¹)	σ_{nuc} (km s ⁻¹)	Υ_V [[Υ_V] _⊙]	β
VCC 452	1380	1.0 ± 1.7	23.8	7.7	5.28 ± 0.82	-0.27 ± 0.23
VCC 917/IC 3344	1186	0.4 ± 0.4	31.1	...	3.41 ± 0.14	-0.87 ± 0.15
VCC 1073/IC 794	1862	2.1 ± 0.4	44.6	31.7	5.83 ± 0.17	-0.64 ± 0.08
VCC 1254	1220	0.9 ± 0.9	31.0	48.6	5.99 ± 0.17	-2.56 ± 0.98
VCC 1577	361	1.3 ± 0.7	26.8	9.8	5.76 ± 0.86	-0.07 ± 0.17
VCC 1876/IC 3658	95	1.2 ± 1.4	25.7	16.5	3.33 ± 0.83	0.10 ± 0.23

Note. — The heliocentric systemic velocity v_{sys} is determined from the mean of each velocity profile. The rotation speed v_{rot} listed in most cases is an upper limit; σ_{gal} is the average line-of-sight velocity dispersion outside $r > 1''$; σ_{nuc} is the calculated projected velocity dispersion of a Plummer profile fit to the dE nucleus, assuming it has the same mass-to-light ratio (Υ_V) as the underlying galaxy; Υ_V , the anisotropy parameter β , and their corresponding errors are determined from the dynamical modeling discussed in § 3.2.2.

Table 5. Fundamental Plane κ -Space Parameters

Galaxy	Underlying dE Galaxy			dE Nuclei		
	κ_1	κ_2	κ_3	κ_1	κ_2	κ_3
VCC 452	1.84	2.45	0.78	-0.11	3.33	0.87
VCC 917/IC 3344	2.07	2.80	0.63
VCC 1073/IC 794	2.29	3.05	0.79	0.71	4.93	0.85
VCC 1254	2.13	2.45	0.83	1.04	5.26	0.86
VCC 1577	1.93	2.45	0.82	0.03	3.61	0.85
VCC 1876/IC 3658	1.94	2.64	0.70	0.24	4.53	0.71

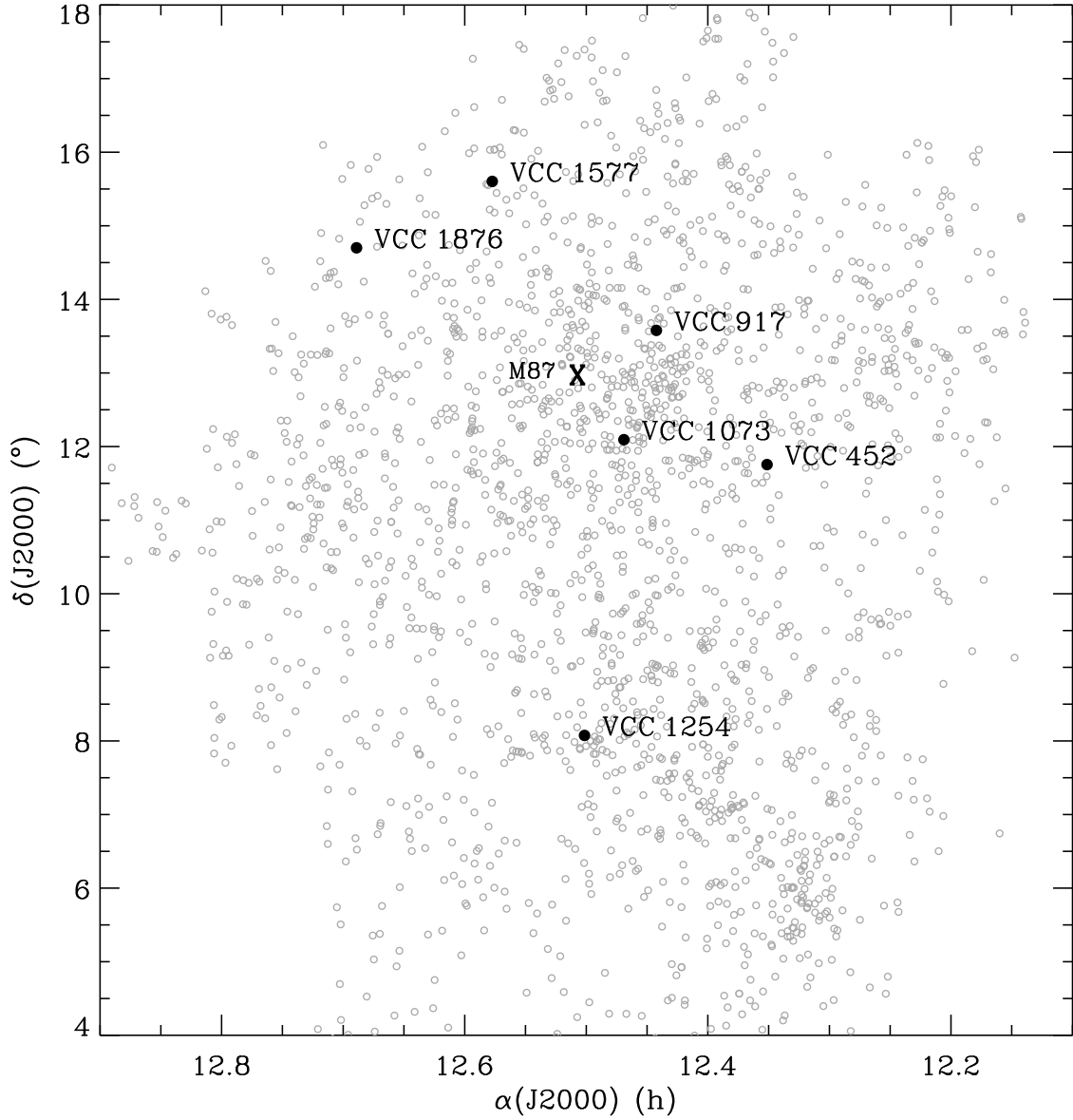


Fig. 1.— Positions (J2000) of the six target Virgo Cluster dE galaxies on the sky (solid circles) relative to all cluster members (open circles) as identified by Bingelli et al. (1985). The “X” symbol indicates the position of M87 at the center of the Virgo cluster.

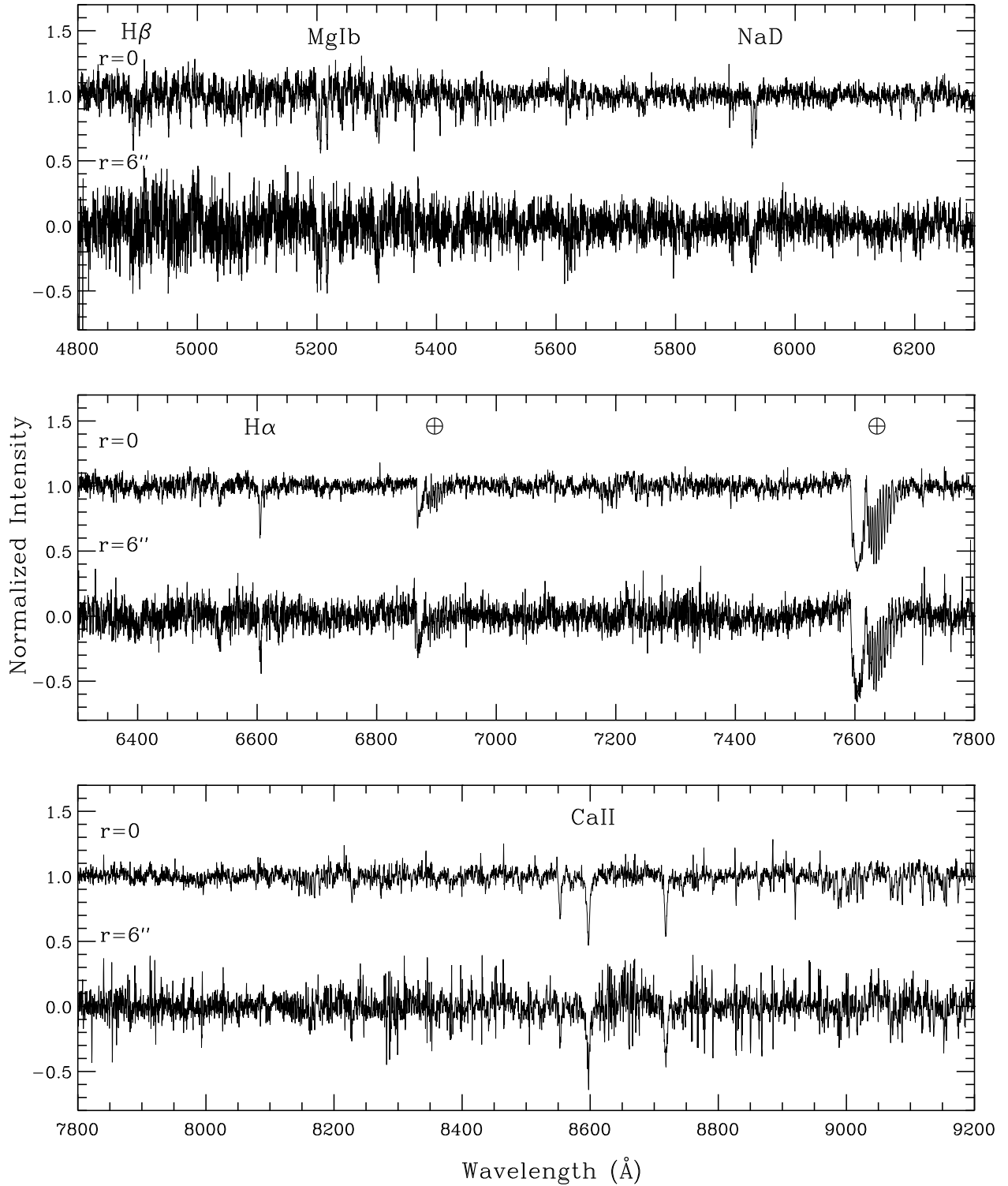


Fig. 2.— Representative Keck/ESI spectra covering the continuous wavelength region $\lambda\lambda 4800\text{--}9200\text{\AA}$ used in determining kinematic profiles for our target galaxies. Spectra of VCC 1073 are shown for the central ($r = 0''$) and outer ($r = 6''$) kinematic data positions. The spectra are binned spatially to $0.8''$, the size of the seeing disk at the time of observations, but have not been smoothed in the spectral direction. A few of the important stellar absorption features in the dE are indicated, along with the atmospheric A and B absorption bands.

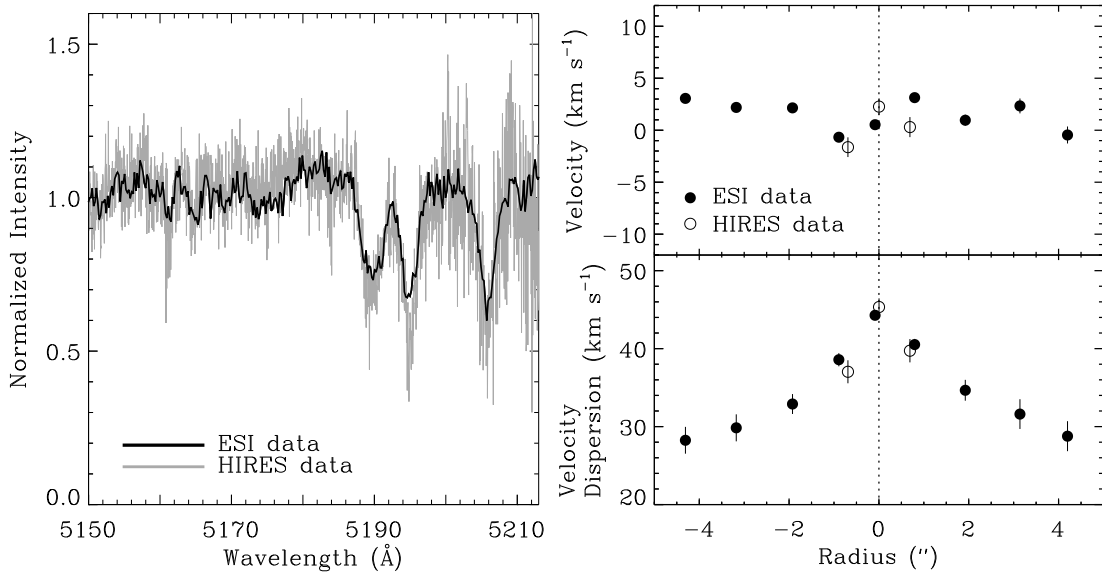


Fig. 3.— *Left*: A spectral comparison of VCC 1254 in the region of the MgIb lines as observed by the ESI (black line) and HIRES (grey line) spectrographs on the Keck telescope. The spectra cover the same spatial region, the central $1''$ of the galaxy. *Right*: Mean radial velocity offset relative to the galaxy’s systemic velocity (*upper right*) and line-of-sight velocity dispersion (*lower right*) as a function of radius along the major axis as determined by ESI (solid circles) and HIRES (open circles) along with 1σ error bars, calculated in the wavelength region $\lambda\lambda 5000\text{--}5250\text{\AA}$. The two datasets are in excellent agreement despite differences in instrumental resolution and S/N ratio.

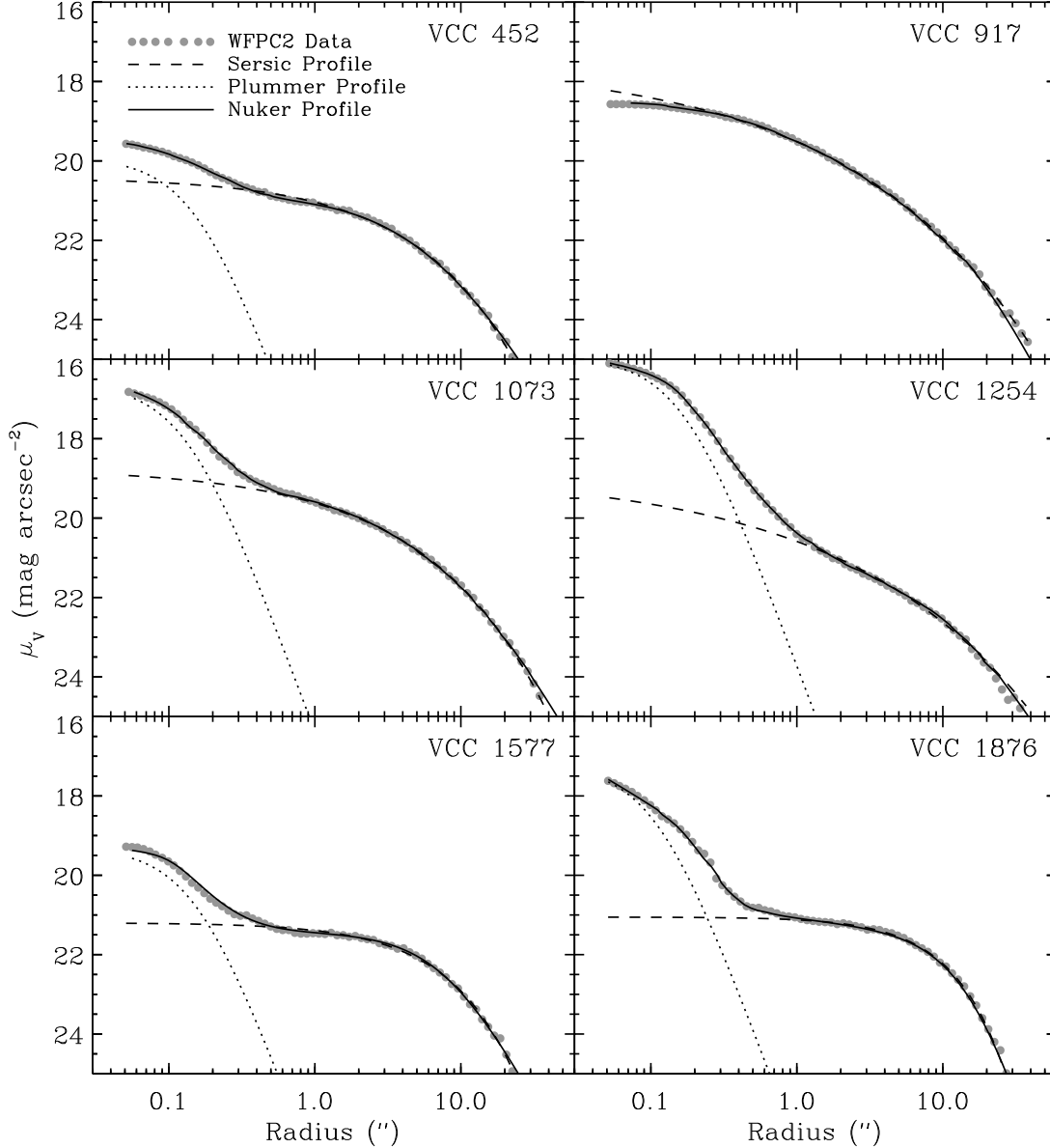


Fig. 4.— Surface brightness profiles as a function of semimajor axis in the V -band derived from *HST* F555W WFPC2 images for the six Virgo dE galaxies (solid grey circles) and analytic profile fits: generalized “Nuker” law (Lauer et al. 1995) fit to the overall profile (solid line), Sersic profile fit to the region outside $1''$ (dashed line), and Plummer profile fit to the inner region of the nucleated galaxies taking into account the *HST* WFPC2 PSF (dotted line; all except VCC 917). Error bars on the observed profiles are smaller than the data points.

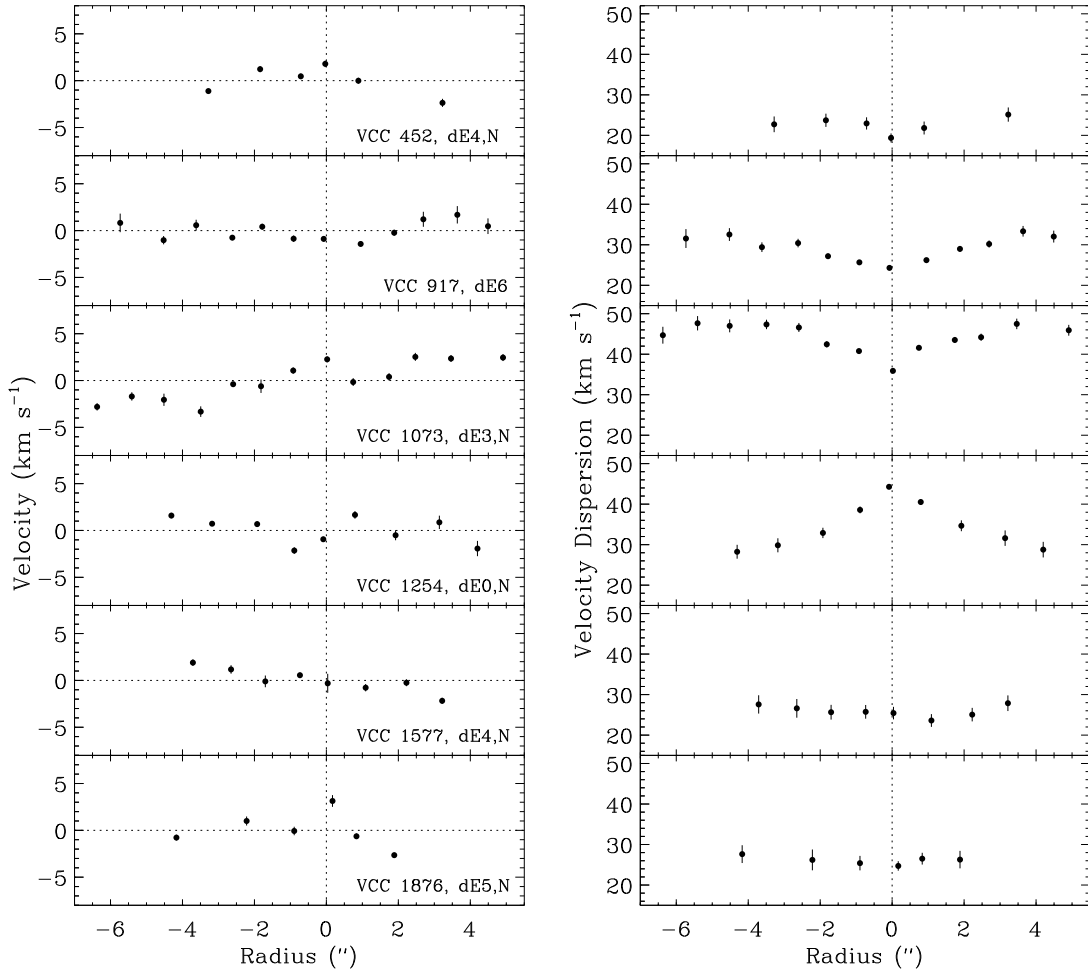


Fig. 5.— The mean line-of-sight velocity offset relative to the galaxy’s systemic velocity (*left panel*) and velocity dispersion (*right panel*) as a function of radial distance along the major axis for the six Virgo dEs observed with ESI. At the distance of Virgo, 1'' corresponds to ~ 100 pc. None of the dEs shows significant rotation with the possible exception of VCC 1073 and VCC 1577. The nuclear velocity dispersion is greater than that of the underlying galaxy in the case of VCC 1254, and smaller in the cases of VCC 452 and VCC 1073.

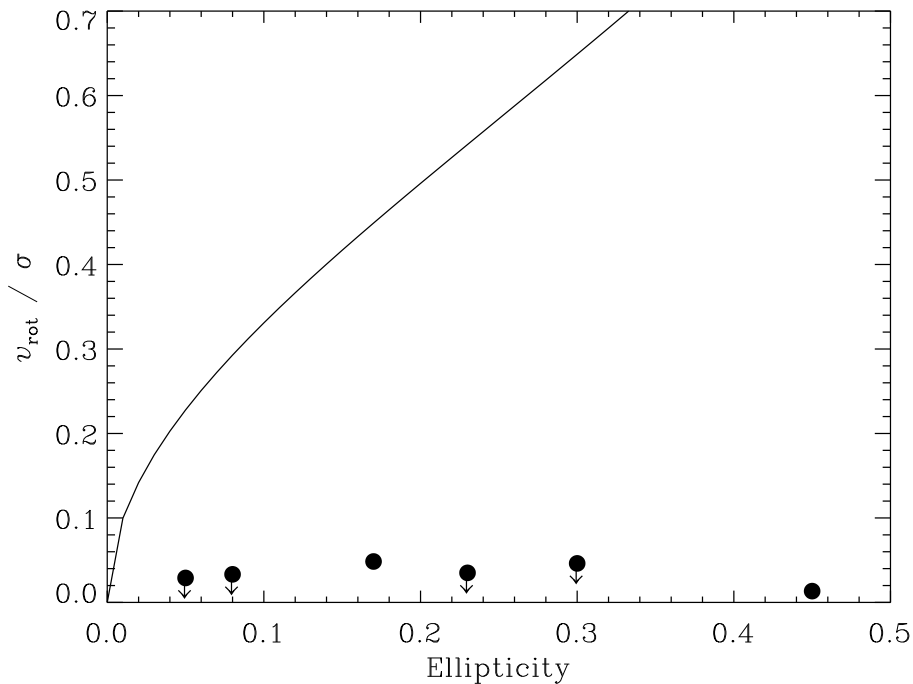


Fig. 6.— The ratio of the upper limit on the rotation velocity v_{rot} to the observed velocity dispersion σ plotted versus mean isophotal ellipticity for six Virgo dE galaxies. The symbols without upper limit arrows are the two dEs which appear to have some rotation, VCC 1073 and VCC 1577. The solid line is the expected relation for an oblate, isotropic galaxy flattened by rotation, seen edge-on; systems that are not edge-on should have somewhat larger predicted v_{rot}/σ values (§ 3.1). The six dEs in our sample do not appear to be rotationally flattened.

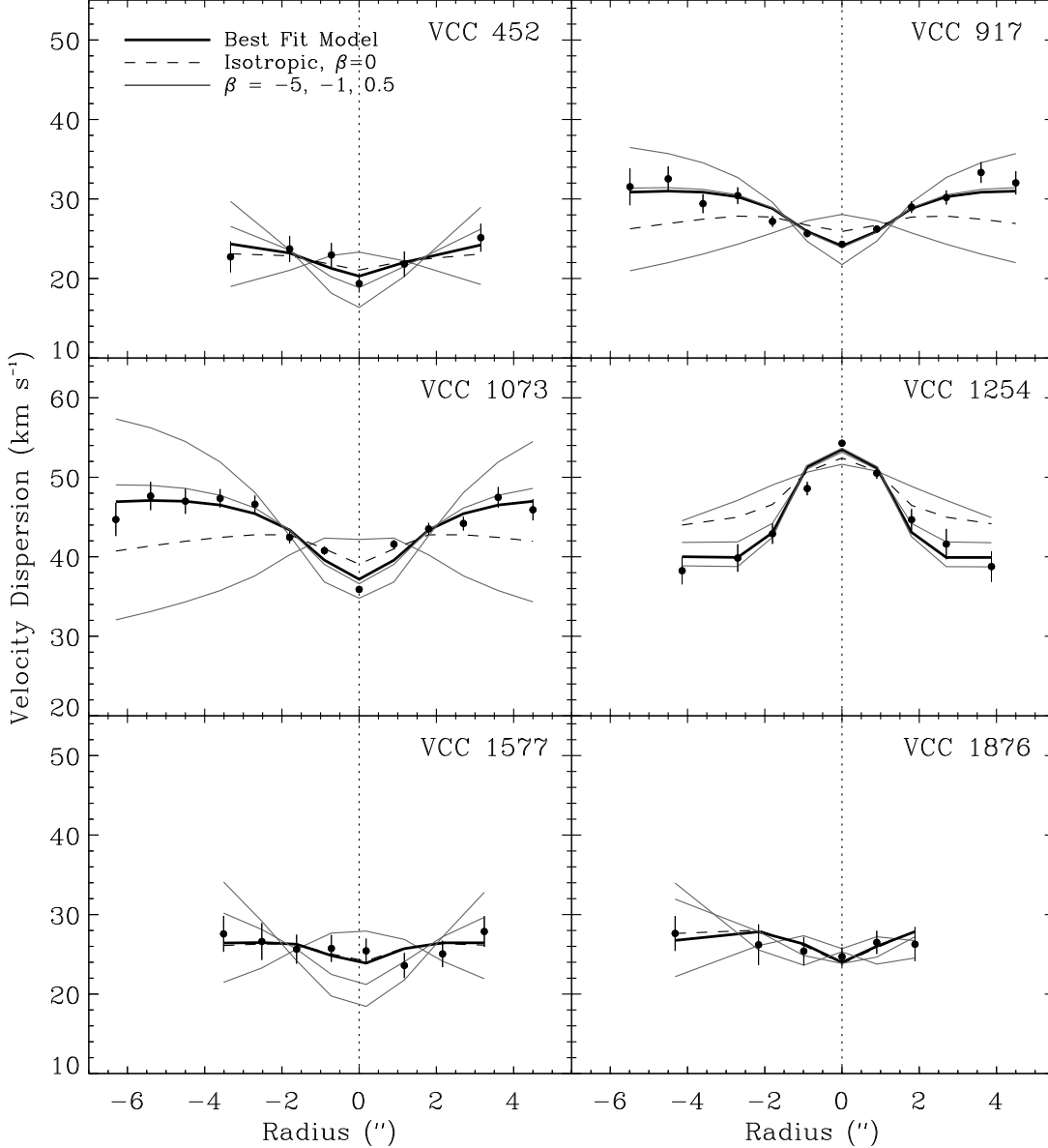


Fig. 7.— Observed line-of-sight velocity dispersion as a function of major axis radius (points with $\pm 1\sigma$ error bars), compared to the predictions of dynamical models with constant velocity anisotropy. The thick solid line indicates the best fit model. For each galaxy, models with $\beta = -5, -1,$ and 0.5 (thin solid lines) and isotropic $\beta = 0$ models (dashed lines) are indicated. The global mass-to-light ratio is optimized via minimization of χ^2_{σ} for each β value (§ 3.2.2). The first four galaxies are fit by tangentially-anisotropic models, while the last two are fit by nearly isotropic models.

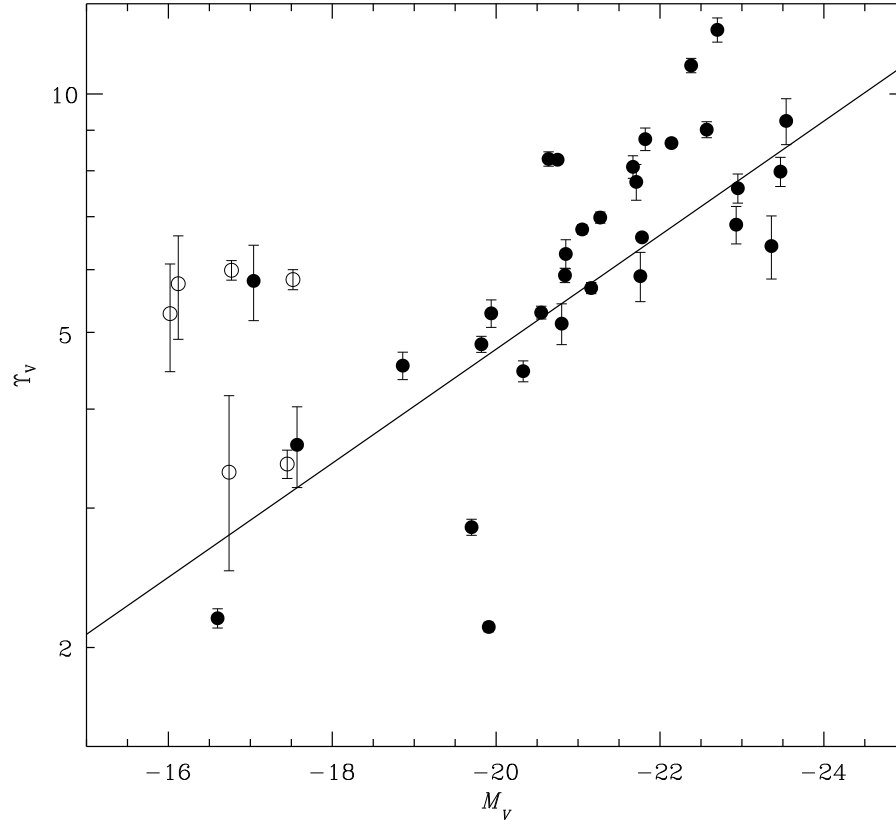


Fig. 8.— Mass-to-light ratio in the V -band Υ_V versus total absolute magnitude for the observed Virgo dE galaxies (open circles) as compared to higher luminosity classical ellipticals (solid circles) of Magorrian et al. (1998). The solid line indicates the Fundamental Plane correlation $\Upsilon_V \propto L_V^{0.2}$ fit to the classical ellipticals.

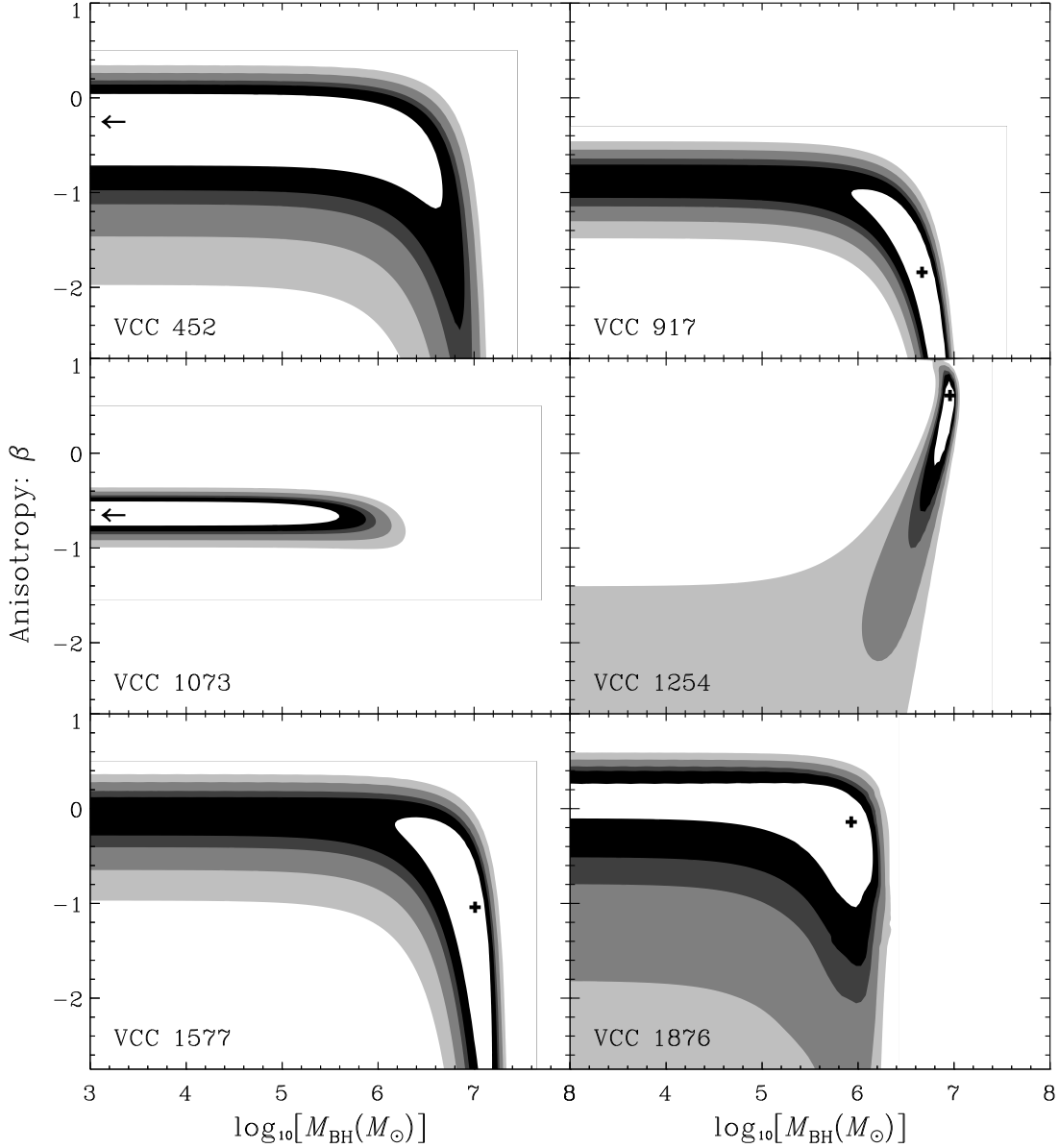


Fig. 9.— Confidence contours for our sample of six Virgo dE galaxies based on fits of dynamical models with constant velocity anisotropy β and a central black hole mass (§ 3.2.3): 68%, 90%, 95%, 99%, and 99.9%. The “+” symbol indicates the best fitting model parameters; an arrow indicates that the best fit is for a zero black hole mass. Black hole masses greater than $M_{\text{BH}} > 10^7 M_{\odot}$ can be ruled out at the 99.9% confidence level for all galaxies.

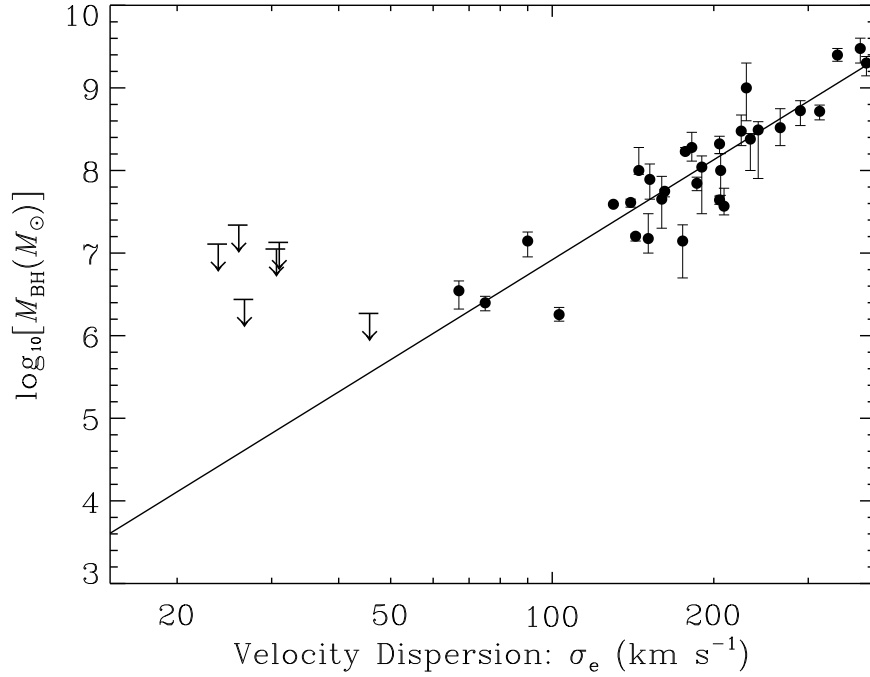


Fig. 10.— Upper limits on the central black hole mass for the observed Virgo dE galaxies (downward arrows) compared to the relationship between black hole mass and bulge velocity dispersion σ_e (solid line) determined by Tremaine et al. (2002) for ellipticals and bulge-dominated spiral galaxies (solid circles). The upper limits on M_{BH} for our Virgo dE galaxies are consistent with the extrapolation of the linear relation fit to the more luminous early-type systems.

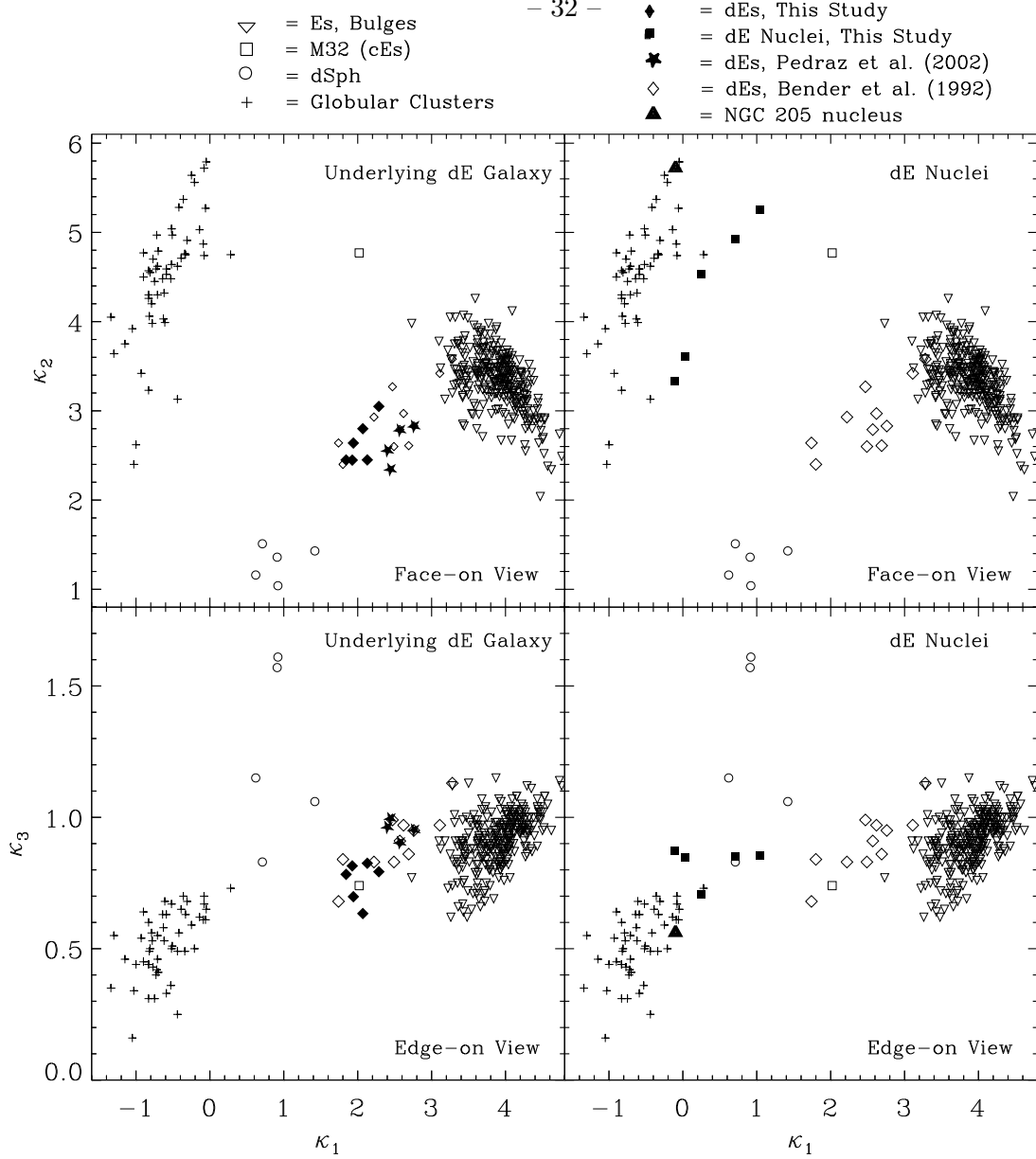


Fig. 11.— Face-on and edge-on projections of the Fundamental Plane for dynamically hot stellar systems (*upper and lower panels, respectively*), where κ_1 , κ_2 , κ_3 are related to galaxy mass, surface brightness, and mass-to-light ratio, respectively. Solid diamonds (*left panels*) represent the underlying dE galaxy (minus the nucleus) for our six Virgo targets; our non-rotating dEs have somewhat smaller masses and M/L ratios than those with substantial rotation studied by Pedraz et al. (2002) (solid stars). The five observed dE nuclei are plotted as solid squares in the right panels as they would appear outside their host galaxy; they are compared to the nucleus of the Local Group dE NGC 205 (solid triangle). Data for other systems from Burstein et al. (1997) are (repeated in left and right panels): classical ellipticals and spiral bulges (open triangles), the compact elliptical M32 (open square), Local Group and other dEs (open diamonds), Local Group dwarf spheroidals (open circles), and Galactic globular clusters (crosses). The dE nuclei appear to be similar to luminous globular clusters.